

---

---

# Whole-Body PET/MR Imaging: Quantitative Evaluation of a Novel Model-Based MR Attenuation Correction Method Including Bone

Daniel H. Paulus<sup>1</sup>, Harald H. Quick<sup>1-3</sup>, Christian Geppert<sup>4</sup>, Matthias Fenchel<sup>4</sup>, Yiqiang Zhan<sup>5</sup>, Gerardo Hermsillo<sup>5</sup>, David Faul<sup>6</sup>, Fernando Boada<sup>7,8</sup>, Kent P. Friedman<sup>7</sup>, and Thomas Koesters<sup>7,8</sup>

<sup>1</sup>Institute of Medical Physics, Friedrich-Alexander-University Erlangen-Nürnberg (FAU), Erlangen, Germany; <sup>2</sup>Erwin L. Hahn Institute for MR Imaging, University Duisburg-Essen, Essen, Germany; <sup>3</sup>High Field and Hybrid MR Imaging, University Hospital Essen, Essen, Germany; <sup>4</sup>Siemens AG Healthcare, Erlangen, Germany; <sup>5</sup>Siemens AG Healthcare, Malvern, Pennsylvania; <sup>6</sup>Siemens AG Healthcare, New York, New York; <sup>7</sup>Bernard and Irene Schwartz Center for Biomedical Imaging, Department of Radiology, New York University School of Medicine, New York, New York; and <sup>8</sup>Center for Advanced Imaging Innovation and Research (CAI2R), New York, New York

---

In routine whole-body PET/MR hybrid imaging, attenuation correction (AC) is usually performed by segmentation methods based on a Dixon MR sequence providing up to 4 different tissue classes. Because of the lack of bone information with the Dixon-based MR sequence, bone is currently considered as soft tissue. Thus, the aim of this study was to evaluate a novel model-based AC method that considers bone in whole-body PET/MR imaging.

**Methods:** The new method ("Model") is based on a regular 4-compartment segmentation from a Dixon sequence ("Dixon"). Bone information is added using a model-based bone segmentation algorithm, which includes a set of prealigned MR image and bone mask pairs for each major body bone individually. Model was quantitatively evaluated on 20 patients who underwent whole-body PET/MR imaging. As a standard of reference, CT-based  $\mu$ -maps were generated for each patient individually by nonrigid registration to the MR images based on PET/CT data. This step allowed for a quantitative comparison of all  $\mu$ -maps based on a single PET emission raw dataset of the PET/MR system. Volumes of interest were drawn on normal tissue, soft-tissue lesions, and bone lesions; standardized uptake values were quantitatively compared. **Results:** In soft-tissue regions with background uptake, the average bias of SUVs in background volumes of interest was  $2.4\% \pm 2.5\%$  and  $2.7\% \pm 2.7\%$  for Dixon and Model, respectively, compared with CT-based AC. For bony tissue, the  $-25.5\% \pm 7.9\%$  underestimation observed with Dixon was reduced to  $-4.9\% \pm 6.7\%$  with Model. In bone lesions, the average underestimation was  $-7.4\% \pm 5.3\%$  and  $-2.9\% \pm 5.8\%$  for Dixon and Model, respectively. For soft-tissue lesions, the biases were  $5.1\% \pm 5.1\%$  for Dixon and  $5.2\% \pm 5.2\%$  for Model. **Conclusion:** The novel MR-based AC method for whole-body PET/MR imaging, combining Dixon-based soft-tissue segmentation and model-based bone estimation, improves PET quantification in whole-body hybrid PET/MR imaging, especially in bony tissue and nearby soft tissue.

**Key Words:** PET/MR hybrid imaging; MR-based attenuation correction; model-based attenuation correction; attenuation correction of bone

**J Nucl Med 2015; 56:1061-1066**

DOI: 10.2967/jnumed.115.156000

---

**A**ttenuation correction (AC) of PET is an essential step in obtaining accurate and quantitative PET images. With the successful introduction of whole-body hybrid imaging systems combining PET with CT (1) or MR imaging (2), it has become possible to perform AC using methods other than rod-source transmission scans. In PET/CT systems, CT images can be directly transformed to linear attenuation coefficients (LACs) at 511 keV, the PET photon energy, using a bilinear conversion (3). In PET/MR systems, PET AC is a technical challenge (4,5) because MR images, providing mainly proton densities, cannot be directly converted to attenuation coefficient maps ( $\mu$ -maps) at 511 keV.

In routine PET/MR imaging, segmentation methods based on a fast 3-dimensional MR Dixon sequence are used to generate  $\mu$ -maps. These methods provide up to 4 tissue classes, including air, fat, lung, and soft tissue (6,7). This method is in wide use for clinical PET/MR studies because of its short acquisition time and easy implementation (8-10), but it has certain limitations compared with CT-based AC. The limited MR imaging field of view, for example, truncates the MR-based  $\mu$ -map (11,12), and the lack of signal in common MR acquisition techniques results in an ambiguity between bone and air on the generated image. Four-compartment segmentation sets the LAC of bone to that of soft tissue, leading to a systematic underestimation in PET standardized uptake values (SUVs) because of the cutoff at  $0.1 \text{ cm}^{-1}$ .

For whole-body PET/MR imaging, several groups have quantitatively evaluated the effect of replacing the LACs of bones with an LAC of soft tissue in PET AC. All studies are based on PET/CT datasets, and the CT images have been modified by thresholding to simulate a segmentation-based MR  $\mu$ -map before being transformed to LACs at 511 keV. Martinez-Möller et al. (6) calculated a bias of  $-8\%$  in bone lesions with a segmentation-based  $\mu$ -map,

---

Received Feb. 18, 2015; revision accepted May 18, 2015.

For correspondence or reprints contact: Daniel H. Paulus, Institute of Medical Physics (IMP), Henkestrasse 91, University of Erlangen-Nürnberg, Erlangen 91052, Germany.

E-mail: daniel.paulus@imp.uni-erlangen.de

Published online May 29, 2015.

COPYRIGHT © 2015 by the Society of Nuclear Medicine and Molecular Imaging, Inc.

Schulz et al. (7) evaluated an underestimation of  $-6.5\%$ , and Samarin et al. (13) reported a bias of  $-11.2\%$  in osseous lesions. Hofmann et al. (14) evaluated a bias of  $-14.1\%$  in normal tissue and  $-7.5\%$  in lesions.

For head imaging, several approaches have been proposed to include cortical bone as an attenuation class using either a combination of atlas registration and pattern recognition (15) or pseudo CTs generated with an ultrashort echo time MR sequence (16). Because of the limited field of view and rather long acquisition time of the ultrashort echo time sequence, this method has not yet been assigned to whole-body PET/MR imaging (16). The atlas- and pattern-recognition-based method was introduced for whole-body imaging (15) but was tested only on PET/CT data in combination with an MR-only acquisition that had been transferred to the PET/CT dataset. With this method, the bias was reduced to  $-8\%$  and  $-6\%$  for normal tissue and lesions, respectively.

Thus, the aim of this study was to evaluate a prototype model-based AC method in hybrid PET/MR imaging that considers major bones in addition to the head on whole-body PET/MR to improve PET/MR AC and specifically the PET quantification in bone lesions and lesions close to bone. The method was tested on 20 patients and compared with routine Dixon-based AC and a CT-based AC generated for each patient individually. All patient data were reconstructed only from the raw PET data of the PET/MR

system, using identical scanner hardware and identical reconstruction settings. Thus, unlike previously published quantitative comparisons of PET/MR and PET/CT data, all influences other than the  $\mu$ -maps were eliminated.

## MATERIALS AND METHODS

### Patient Population

Within this study, 20 patients (mean age  $\pm$  SD,  $54.8 \pm 16.8$  y; range, 25–85 y; 19 women and 1 man) underwent a clinically indicated PET/CT examination and a subsequent whole-body PET/MR acquisition. The patients provided written informed consent, and the approval of the institutional review and ethical board was obtained. No additional radiotracer was injected for the PET/MR acquisition. Relevant patient information is listed in Table 1.

### Imaging Protocol

All patients underwent PET/CT (Biograph mCT; Siemens AG Healthcare) according to the standard clinical protocol. The average injected activity was  $541.7 \pm 18.4$  MBq. Because all PET reconstructions within this study were based on PET/MR datasets, the PET unit is not further described, but CT images of those datasets were used within this study. The PET/CT system comprises a 40-slice CT detector, and CT was performed using a setting of 100–140 kVp, a pixel size of  $1.52 \times 1.52$  mm or  $1.37 \times 1.37$  mm, and a slice thickness of 5.0 mm.

**TABLE 1**  
Patient Characteristics

Patient no.	Age (y)	Weight (kg)	Injected activity (MBq)	Active lesions that have been evaluated
1	66	63	562	—
2	68	50	524	Subcarinal LN, spinous process bone metastasis, R hilar LN, R T4 transverse process bone metastasis, left lung mass
3	75	60	558	R femoral head bone metastasis
4	51	56	542	L peritoneum, gastrohepatic LN, L diaphragm after implantation
5	69	101	528	—
6	41	70	554	—
7	28	57	554	T spine, upper T spine vertebral body, R L5 bone, L iliac bone metastasis, R iliac bone metastasis
8	49	63	562	R lung base, L mid lung, L upper lung
9	54	104	534	L axillary LN
10	46	54	548	R hilar LN
11	52	63	535	—
12	50	68	557	Liver metastasis
13	32	61	544	R breast mass, R axillary LN metastasis
14	83	43	502	Subcarinal LN, Right hilar LN, L hilar LN
15	25	56	505	L breast mass
16	60	66	560	—
17	48	82	554	Peritoneal implant
18	85	75	521	—
19	47	54	534	—
20	66	63	557	L spine vertebral body, L spine vertebral body, T spine vertebral body

LN = lymph node; T = thoracic.

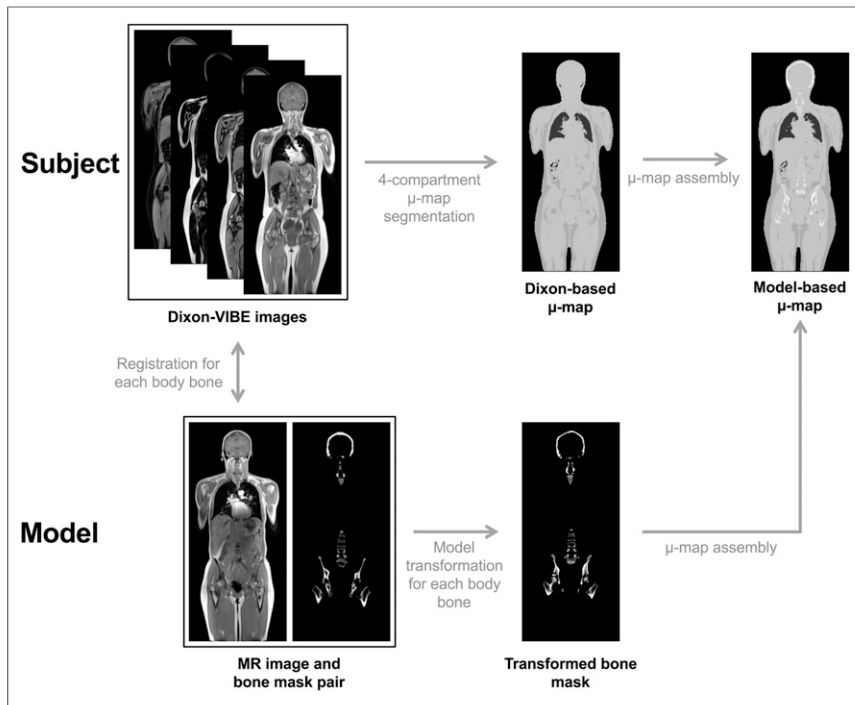


**FIGURE 1.** Schematic drawing of model-based algorithm for considering bone in whole-body PET/MR AC. The model consists of set of MR image and bone mask pairs that are registered to subject's Dixon-VIBE images for each body bone individually. Transformation is applied to bone segmentation for each body bone and added to 4-compartment segmentation-based  $\mu$ -map at all voxels of densities higher than soft tissue.

PET/MR was performed on a 3-T whole-body system (Biograph mMR; Siemens Healthcare) that comprises a fully integrated PET detector in its isocenter with a field of view of 25.8 cm in the  $z$  direction.

The average time between injection and PET/MR acquisition was  $200.3 \pm 48.8$  min. Fourteen patients were examined using 5 bed positions. Six patients were examined using 3 bed positions, in which the head was not included in the PET/MR protocol, but the datasets were still relevant for the whole-body study.

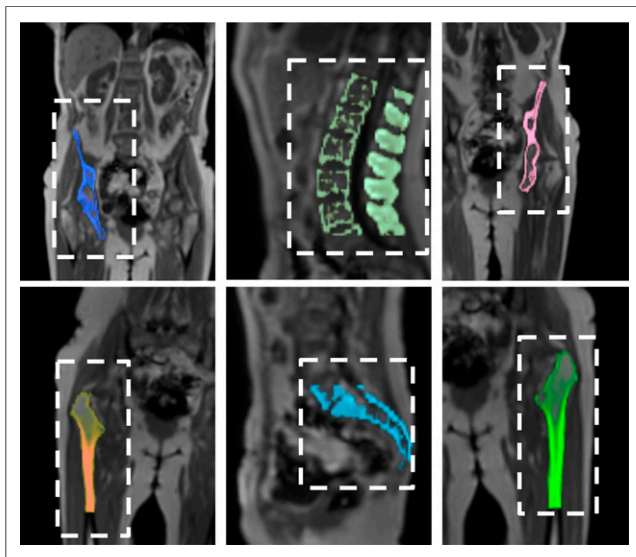


**FIGURE 2.** Schematic of crop of local bone masks that contain bone densities as LACs in  $\text{cm}^{-1}$  at 511 keV in subject MR image. Dashed boxes indicate specific bones being cropped from image.

## PET/MR $\mu$ -maps

The PET data acquired with the PET/MR system were reconstructed using 3 different  $\mu$ -maps for each subject: standard PET/MR Dixon-based AC ("Dixon"), the new model-based AC ("Model"), and a CT-based AC that was generated for each patient individually and used as the standard of reference. Because all PET data were based on a single emission data file, using identical parameters such as scanner hardware and reconstruction settings, all influences other than the  $\mu$ -map were eliminated.

*Dixon.* Dixon was performed with 2-point, 3-dimensional volume-interpolated breath-hold examination (VIBE). The soft-tissue segmentation algorithm provides 4 different tissue classes: air (LAC,  $0.0 \text{ cm}^{-1}$ ), fat (LAC,  $0.0854 \text{ cm}^{-1}$ ), lung (LAC,  $0.0224 \text{ cm}^{-1}$ ), and soft tissue (LAC,  $0.1 \text{ cm}^{-1}$ ). The sequence parameters per bed position were as follows: voxel dimensions,  $192 \times 126$  with 128 slices in the coronal orientation; voxel size,  $2.60 \times 2.60 \text{ mm}$  with a slice thickness of 3.12 mm; repetition time, 3.6 ms; echo time, 2.46 ms; flip angle,  $10^\circ$ ; and acquisition time, 19 s.

*Model.* The new Model approach is illustrated in Figure 1. The method generates a  $\mu$ -map based on standard Dixon AC. Bone information is added to this  $\mu$ -map using a model-based prototype bone segmentation algorithm (Siemens AG Healthcare) that applies continuous LACs for bone. The offline-constructed

model includes a set of prealigned MR image and bone mask pairs for each major body bone, including left and right upper femur, left and right hip, spine (including sacrum), and skull. Bone masks contain bone densities as LACs in  $\text{cm}^{-1}$  at the PET energy level of 511 keV. At run-time, the MR image of the model is registered to the MR image of the subject at each major body bone individually. The bone is segmented by registering a given image to the MR model with known bone mask and transferring the bone model.

The registration algorithm consists of 2 stages, landmark-based similarity registration and intensity-based deformable registration. In the landmark-based similarity registration, a learning-based approach is applied to detect a set of landmarks surrounding each bone (17). These landmarks are used in 2 ways. First, they are used to crop specific bones from the subject image as shown in Figure 2. Second, for each bone, a least-square solver is applied to derive the similarity transformation between the subject and the model based on the locations of these landmarks. After the similarity registration, a more sophisticated deformable registration (18) is performed to bring the model to the subject space more precisely. In essence, this method maximizes the cross-correlation between the subject images and the model images. Different Dixon sequence information is used at different stages of the registration framework. Although the out-of-phase and fat images are used in the first stage, in-phase and fat images are used in the second stage. The prealigned bone masks are then brought to the subject space following the same transformations. The bone density information is added to the original Dixon-based  $\mu$ -map at all voxels higher in density than soft tissue after the segmentation process. LACs for bone were in the range of 0.1 and  $0.2485 \text{ cm}^{-1}$  depending on the bone mask pair. The average running time of the algorithm was between 2 and 3 min per whole-body dataset.

The bone model was generated offline from a pool of more than 200 Dixon-VIBE MR images and bone mask pairs. Bone masks were chosen from the pool on the basis of the shape and density best

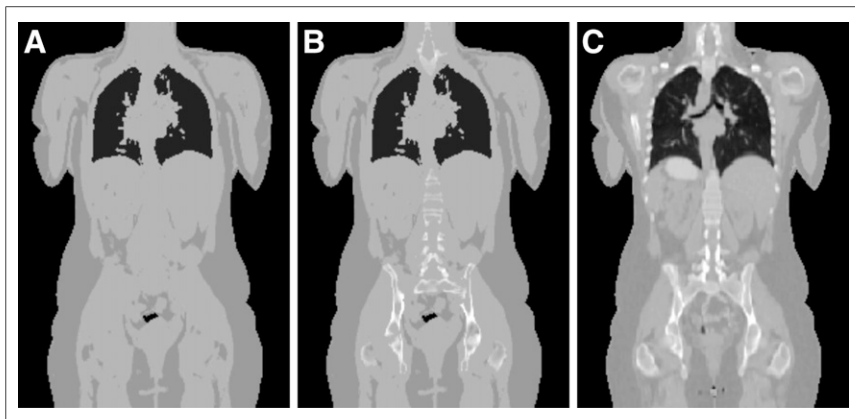


**FIGURE 3.** Example Dixon (A), Model (B), and CT (C)  $\mu$ -maps.

representing the average of the pool. All patients underwent clinically indicated PET/CT and, with no further radiotracer injection, follow-up PET/MR imaging.

**CT.** To minimize physiologic and intersystem quantification biases, the standard-of-reference baseline was computed from the PET/MR emission data, where MR-based AC was replaced by standard CT-based AC. Therefore, CT images based on the PET/CT data of the same subject were nonrigidly registered to the anatomic Dixon-VIBE images and visually compared to ensure optimal anatomic alignment using a registration framework similar to that of Model. It consists of 2 stages, a landmark-based rigid registration (17) and a deformable registration (18). To provide LACs at 511 keV, the CT images were transformed using the standard bilinear conversion (3). Because PET/CT acquisitions were performed with arms up and not with arms down as in PET/MR, the missing parts of each patient, mainly the arms in the outer part of the field of view, were added from the MR-based Dixon-VIBE  $\mu$ -map.

#### Data Processing

PET images were reconstructed iteratively on the PET/MR system with 3-dimensional ordinary Poisson ordered-subsets expectation maximization using 3 iterations and 21 subsets. The image matrix was set to  $172 \times 172$  with a pixel size of  $4.173 \times 4.173$  mm as used for

standard whole-body PET/MR acquisitions. Patients were scanned and reconstructed for either 5 bed positions (515 slices) or 3 bed positions (321 slices) with a slice thickness of 2.031 mm. All patient  $\mu$ -maps were postprocessed with an algorithm (maximum-likelihood reconstruction of attenuation and activity) to add the missing parts of the arms. All PET images were postsmoothed with a gaussian filter having a full width at half maximum of 4 mm.

#### PET Evaluation

The PET images were evaluated using MIMfusion, version 6.3 (MIM Software Inc.). Volumes of interest (VOIs) were manually drawn on normal tissue using superimposed MR images of a radial T1-weighted VIBE sequence that is used as the diagnostic MR sequence in whole-body PET/MR acquisitions.

The mean SUV ( $SUV_{mean}$ ) was calculated for the following VOIs: aorta/blood level (15-mm sphere), liver (30-mm sphere), spleen (20-mm sphere), femoral head left/right (25-mm sphere), iliac bones left/right (dynamic brush), psoas muscles left/right (dynamic brush), third lumbar vertebra (L3, 20-mm sphere), and subcutaneous fat (variable VOI sizes). Furthermore, VOIs were drawn on all identified lesions—soft-tissue lesions as well as bone lesions—in all 20 subjects using a 50% maximum contour of the PET SUV. For all PET evaluations, the  $SUV_{mean}$  of the CT AC was used as a standard of reference, and the percentage deviation was calculated for normal tissue across all 20 subjects for Dixon and Model.

Of all VOIs in normal tissues, 1 femoral head and 1 iliac bone of 2 patients were excluded because of hip implants. Furthermore, 1 femoral head VOI and 2 iliac bone VOIs were excluded because of lesions or metastases inside the VOIs. One spleen VOI is missing because the patient underwent splenectomy.

#### RESULTS

All 3 different  $\mu$ -maps are shown in coronal view in Figure 3, before the postprocessing algorithm was applied.

The diagnostic MR image of the radial T1-weighted VIBE sequence, the PET image, and the superimposed PET/MR image of a patient are shown in Figure 4. Additionally, a maximum-intensity projection of the PET data showing the drawn contours is included.

Mean deviations of  $SUV_{mean}$  in percentage of normal tissue across all 20 subjects are plotted in Figure 5 for Dixon and Model normalized to the corresponding CT  $SUV_{mean}$ . For the background VOIs of soft tissue, such as aorta, liver, spleen, subcutaneous fat, and psoas muscles, the  $SUV_{mean}$  of Dixon and the  $SUV_{mean}$  of Model are almost equivalent, with a maximum deviation of 1.2%. Both methods are close to the CT AC (7.6% maximum deviation with Model). However, cold-background VOIs within bone were underestimated with Dixon by  $-46.5\% \pm 9.3\%$  for femoral head,  $-20.0\% \pm 5.5\%$  for iliac bones, and  $-9.9\% \pm 8.9\%$  for L3. With Model, the underestimation was reduced to  $-4.9\% \pm 7.7\%$ ,  $-2.8\% \pm 4.6\%$ , and  $-7.1\% \pm 7.8\%$ , respectively.

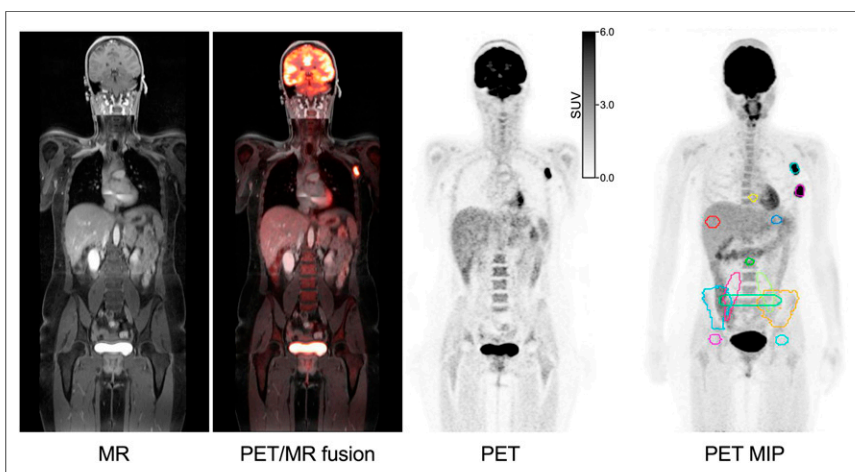


**FIGURE 4.** Diagnostic MR image of radial T1-weighted VIBE sequence, superimposed PET/MR image, PET image, and maximum-intensity projection (MIP) of PET image displaying evaluated contours. Differences in intensity of MR image are due to variances in radiofrequency coil adjustments between bed positions.

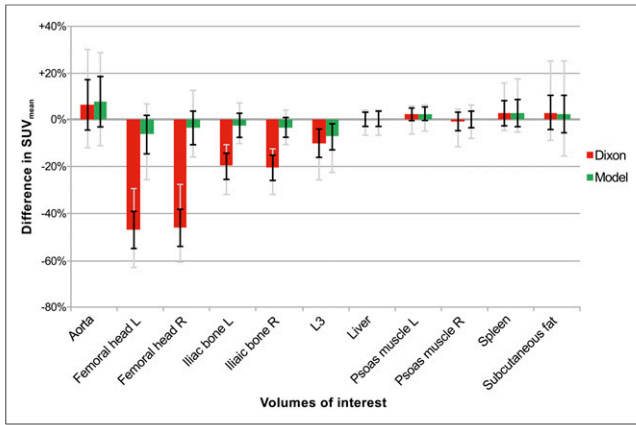


**FIGURE 5.** Percentage difference in PET  $SUV_{mean}$  of normal tissue averaged across all subjects for Dixon (red) and Model (green) compared with CT AC. Vertical bars indicate mean  $\pm$  SD (black) and total range (gray).

Deviations in the  $SUV_{mean}$  of soft-tissue and bone lesions are shown in Figures 6A and 6B, respectively. For soft-tissue lesions, the deviation between Dixon and Model was negligible, with a mean of 0.3% and a maximum of 1.5%. Furthermore, the  $SUV_{mean}$  was overestimated by more than 20% in some regions compared with CT AC.

All these lesions, however, were located either within the lung or near lung tissue. Comparing the CT-based  $\mu$ -map with the segmentation-based  $\mu$ -map for these cases, one can see that soft tissue (LAC,  $0.1 \text{ cm}^{-1}$ ) was assigned to some parts of the lung that were actually lung tissue with an LAC of around  $0.02 \text{ cm}^{-1}$ . If the lesion was within or near these areas, as seen in Figure 7, the SUV of the lesion was highly increased for Dixon and Model compared with CT AC. When these lung cases were excluded from the evaluation, the  $SUV_{mean}$  difference in soft-tissue lesions was  $5.1\% \pm 5.1\%$  and  $5.2\% \pm 5.2\%$  for Dixon and Model, respectively.

For bone lesions, an underestimation of  $-7.3\% \pm 5.3\%$  (maximum,  $-19.4\%$ ) was observable for Dixon compared with CT, and this underestimation was reduced to  $-2.9\% \pm 5.8\%$  (maximum,  $-18.7\%$ ) with Model. Deviations between Dixon and Model were  $4.5\% \pm 2.7\%$ , with a maximum of 9.8%.

## DISCUSSION

On a dataset of 20 PET/MR patients, it was shown that the new Model approach improved PET SUVs in bony regions. Figures 5 and 6B show the benefit of adding bone to the MR-based  $\mu$ -map that is based on segmentation. However, Model seemed to have little impact on normal soft tissue (Fig. 5) or soft-tissue lesions (Fig. 6A).

The calculated SUV underestimation of  $-7.3\%$  in bone lesions with Dixon is comparable to the findings of former whole-body studies (between  $-7\%$  and  $-11\%$ ), which were based on PET/CT instead of PET/MR data (6,7,13). Hofmann et al. (14) reduced the bias to  $-8\%$  and  $-6\%$  for normal tissue and lesions, respectively, with an atlas- and pattern-recognition-based method. However, in their study, the MR  $\mu$ -map was transferred to the PET/CT dataset, and all PET raw data were based on PET/CT. Within our current study, SUV underestimation in bone lesions was reduced to  $-2.9\%$  with Model.

When Model and Dixon were compared with CT AC in normal soft tissue, Model and Dixon were consistent with each other (Fig. 5), having a mean overestimation of 2.4% and 2.7%, respectively. Thus, adding bone to the MR-based segmentation  $\mu$ -map had only a limited impact on SUVs in soft tissues distant from bone, as has

been shown by other groups (6,13). Furthermore, in these regions, the Dixon  $\mu$ -map performed virtually identically to CT AC. This effect was also observable for soft-tissue lesions. Compared with CT, both methods overestimated the SUV by around 30% in some soft-tissue lesions, confirming the findings of Drzezga et al. (8). However, the overestimation was due to segmentation differences that occur if soft tissue (LAC,  $0.1 \text{ cm}^{-1}$ )—instead of lung tissue (LAC,  $0.02 \text{ cm}^{-1}$ )—is assigned to some parts of the lung, as shown in Figure 7. When such lung cases were excluded, the mean bias in soft-tissue lesions was 5.2% and 5.1% for Dixon and Model, respectively. Furthermore, a potential respiratory difference between CT and MR for which registration cannot fully compensate might affect evaluations in the lung.

Besides segmentation biases in the lung, the variation in bone density between patients should be considered. Although variation is expected to be relatively small in patients without bone diseases, bone density changes due to diseases may have a greater impact on PET quantification. SUV may be overestimated within or near bones of decreased density, since the LACs of the model are higher than the actual bone LACs. This limitation, however, applies to most MR-based AC methods, including segmentation- and atlas-based AC. For better matching of bone densities, the model might be improved by being categorized by age, sex, and race.

In contrast to former whole-body PET/MR AC studies, the PET data of each patient within this study were based on only the emission raw dataset of the PET/MR system, which focuses the quantitative comparison on differences in the attenuation maps. Thus, physiologic aspects, such as differences in patient positioning or tracer washout between PET/CT and PET/MR scanning, can be excluded. Also, the attenuation effect of local radiofrequency surface coils, leading to a potential average underestimation of  $-5\%$  to  $-20\%$  when neglected in AC (19,20), can be

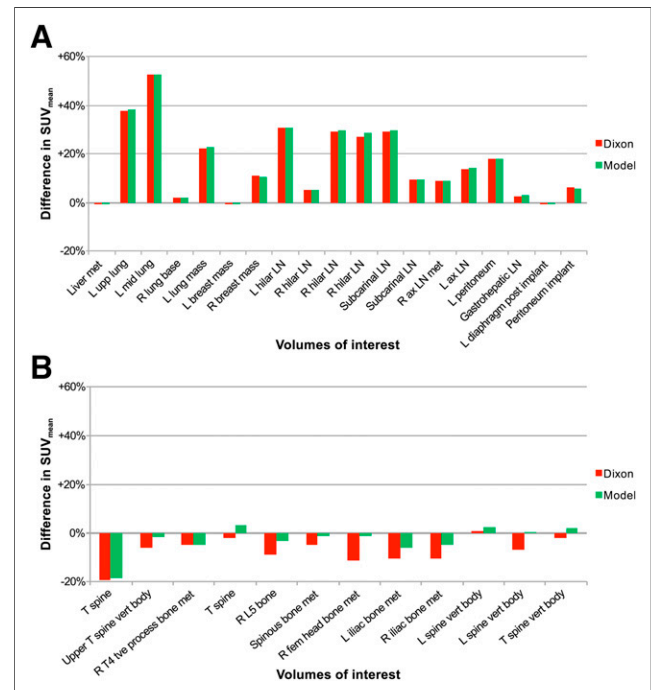


**FIGURE 6.** Percentage difference in PET  $SUV_{mean}$  of indicated soft-tissue lesions (A) and bone lesions (B) in individual patients for Dixon (red) and Model (green) compared with CT AC. ax = axillary; fem = femoral; LN = lymph node; met = metastasis; T = thoracic; tve = transverse; vert = vertebral.

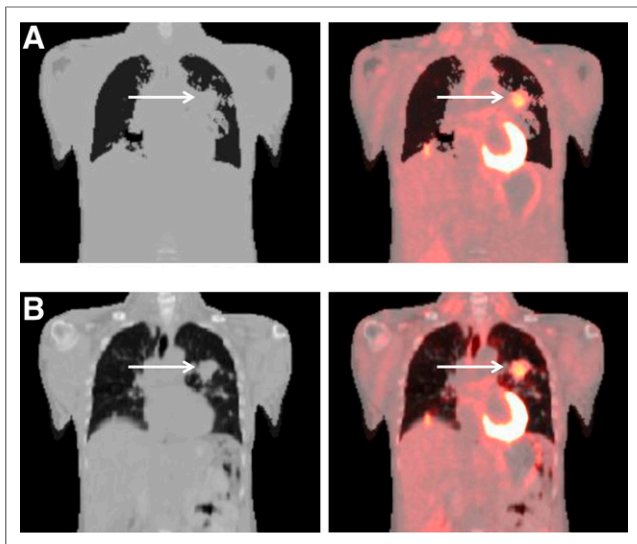


**FIGURE 7.** Coronal images of MR- and CT-based  $\mu$ -maps showing differences in lung that lead to increase in  $SUV_{mean}$  for Dixon and Model compared with CT AC.  $\mu$ -maps are shown both by themselves and superimposed on the PET images. Arrows point toward lesion that showed 53% increase in  $SUV_{mean}$ . Differences between Dixon-VIBE segmentation (A) and CT (B) can be seen. Although CT shows primarily lung tissue (LAC,  $\sim 0.02\text{ cm}^{-1}$ ) around active lesion, this area is assigned to soft tissue (LAC,  $0.1\text{ cm}^{-1}$ ) in MR-based  $\mu$ -map.

excluded because all PET reconstructions are performed with the same settings and raw data. Furthermore, any potential interscanner biases can be excluded if the raw datasets of different PET systems are used in quantitative comparisons.

CT-based  $\mu$ -maps were used as a standard of reference in this study, although missing parts such as the arms were added from the Dixon-based  $\mu$ -map and thus it is not the actual CT  $\mu$ -map that is the reference. However, the main part of the  $\mu$ -map is CT-based, and the remaining part is identical in all 3  $\mu$ -maps of each subject, thus not introducing additional bias. Furthermore, the effect of the arms on VOIs inside the body is expected to be negligible.

Compared with former approaches to including bone information (mainly the head) in PET/MR AC, Model does not require any additional MR sequences such as are needed in, for example, the ultrashort echo time approach (16). Model is based on only the Dixon MR sequence, which is already acquired for routine MR-based AC and has a short run-time of about 2–3 min per whole-body dataset. This advantage, as well as the overall improvement in PET AC and, especially, PET quantification in bone lesions compared with Dixon, shows potential for clinical use of Model in whole-body PET/MR imaging.

## CONCLUSION

This study evaluated a new AC method for whole-body PET/MR imaging that combines the discrete LAC Dixon-based soft-tissue segmentation with a model-based bone estimation providing continuous LACs for bone. The method was shown to improve PET quantification, especially in bony tissue, bone lesions, and tissue near bone, by reducing the SUV underestimation that occurs with the Dixon-based  $\mu$ -map. Because the new method utilizes the MR-based Dixon images, no further MR acquisitions are required. This advantage and an average run-time of 2–3 min per whole-body dataset make the new method promising for clinical application.

## DISCLOSURE

The costs of publication of this article were defrayed in part by the payment of page charges. Therefore, and solely to indicate this fact, this article is hereby marked “advertisement” in accordance with 18 USC section 1734. This work was supported by a research agreement between Siemens AG Healthcare and the University of Erlangen-Nürnberg, Germany. The Center for Advanced Imaging Innovation and Research (CAI2R) at New York University School of Medicine is supported by NIH/NIBIB grant P41 EB017183. This work was performed in (partial) fulfillment of the requirements for obtaining the degree “Dr. rer. biol. hum.” at the Friedrich-Alexander-University Erlangen-Nürnberg (FAU). No other potential conflict of interest relevant to this article was reported.

## REFERENCES

1. Beyer T, Townsend DW, Brun T, et al. A combined PET/CT scanner for clinical oncology. *J Nucl Med.* 2000;41:1369–1379.
2. Delso G, Furst S, Jakoby B, et al. Performance measurements of the Siemens mMR integrated whole-body PET/MR scanner. *J Nucl Med.* 2011;52:1914–1922.
3. Kinahan PE, Townsend DW, Beyer TT, Sashin D. Attenuation correction for a combined 3D PET/CT scanner. *Med Phys.* 1998;25:2046–2053.
4. Bezrukov I, Mantlik F, Schmidt H, Schölkopf B, Pichler BJ. MR-based PET attenuation correction for PET/MR imaging. *Semin Nucl Med.* 2013;43:45–59.
5. Keereman V, Mollet P, Berker Y, Schulz V, Vandenberghe S. Challenges and current methods for attenuation correction in PET/MR. *MAGMA.* 2013;26:81–98.
6. Martinez-Möller A, Souvatzoglou M, Delso G, et al. Tissue classification as a potential approach for attenuation correction in whole-body PET/MRI: evaluation with PET/CT data. *J Nucl Med.* 2009;50:520–526.
7. Schulz V, Torres-Espallardo I, Renisch S, et al. Automatic, three-segment, MR-based attenuation correction for whole-body PET/MR data. *Eur J Nucl Med Mol Imaging.* 2011;38:138–152.
8. Drzezga A, Souvatzoglou M, Eiber M, et al. First clinical experience with integrated whole-body PET/MR: comparison to PET/CT in patients with oncologic diagnoses. *J Nucl Med.* 2012;53:845–855.
9. Wiesmüller M, Quick HH, Navalpakkam BK, et al. Comparison of lesion detection and quantitation of tracer uptake between PET from a simultaneously acquiring whole-body PET/MR hybrid scanner and PET from PET/CT. *Eur J Nucl Med Mol Imaging.* 2013;40:12–21.
10. Quick HH, von Gall CC, Zeilinger M, et al. Integrated whole-body PET/MR hybrid imaging: clinical experience. *Invest Radiol.* 2013;48:280–289.
11. Nuyts J, Bal G, Kehren F, Fenchel M, Michel C, Watson C. Completion of a truncated attenuation image from the attenuated PET emission data. *IEEE Trans Med Imaging.* 2013;32:237–246.
12. Blumhagen JO, Braun H, Ladebeck R, et al. Field of view extension and truncation correction for MR-based human attenuation correction in simultaneous MR/PET imaging. *Med Phys.* 2014;41:022303.
13. Samarin A, Burger C, Wollenweber SD, et al. PET/MR imaging of bone lesions: implications for PET quantification from imperfect attenuation correction. *Eur J Nucl Med Mol Imaging.* 2012;39:1154–1160.
14. Hofmann M, Bezrukov I, Mantlik F, et al. MRI-based attenuation correction for whole-body PET/MRI: quantitative evaluation of segmentation- and atlas-based methods. *J Nucl Med.* 2011;52:1392–1399.
15. Hofmann M, Steinke F, Scheel V, et al. MRI-based attenuation correction for PET/MRI: a novel approach combining pattern recognition and atlas registration. *J Nucl Med.* 2008;49:1875–1883.
16. Navalpakkam BK, Braun H, Kuwert T, Quick HH. Magnetic resonance-based attenuation correction for PET/MR hybrid imaging using continuous valued attenuation maps. *Invest Radiol.* 2013;48:323–332.
17. Zhan Y, Zhou X, Peng Z, Krishnan A. Active scheduling of organ detection and segmentation in whole-body medical images. In: Metaxas D, Axel L, Fichtinger G, Székely G, eds. *Medical Image Computing and Computer-Assisted Intervention: MICCAI 2008.* Berlin, Germany: Springer; 2008:313–321.
18. Hermosillo G, Chef'd'Hotel C, Faugeras O. Variational methods for multimodal image matching. *Int J Comput Vis.* 2002;50:329–343.
19. Paulus DH, Braun H, Aklan B, Quick HH. Simultaneous PET/MR imaging: MR-based attenuation correction of local radiofrequency surface coils. *Med Phys.* 2012;39:4306–4315.
20. Kartmann R, Paulus DH, Braun H, et al. Integrated PET/MR imaging: automatic attenuation correction of flexible RF coils. *Med Phys.* 2013;40:082301.